74. Z. Bao, M.R. Weatherspoon, S. Shian, Y. Cai, P.D. Graham, S.M. Allan, G. Ahmad, M.B. Dickerson, B.C. Church, Z. Kang, H.W. Abernathy III, C.J. Summers, M. Liu, K.H. Sandhage, Chemical reduction of three-dimensional silica micro-assemblies into microporous silicon replicas. Nature **446**, 172–175 (2007)
75. A. Ponzoni, E. Comini, G. Sberveglieri, J. Zhou, S.Z. Deng, N.S. Xu, Y. Ding, Z.L. Wang, Ultrasensitive and highly selective gas sensors using three-dimensional tungsten oxide nanowire networks. Appl. Phys. Lett. **88**, 203101–203103 (2006)
76. D. Zhang, Z. Liu, C. Li, T. Tang, X. Liu, S. Han, B. Lei, C. Zhou, Detection of NO_2 down to ppb levels using individual and multiple In_2O_3 nanowire devices. Nano Lett. **4**, 1919–1924 (2004)
77. Y.L. Bunimovich, Y.S. Shin, W.S. Yeo, M. Amori, G. Kwong, J.R. Heath, Quantitative real-time measurements of DNA hybridization with alkylated nonoxidized silicon nanowires in electrolyte solution. J. Am. Chem. Soc. **128**, 16323–16331 (2006)
78. O. Kuzmych, B.L. Allen, A. Star, Carbon nanotube sensors for exhaled breath components. Nanotechnology **18**, 375502 (2007)
79. M.J. Thorpe, K.D. Moll, R.J. Jones, B. Safdi, J. Ye, Broadband cavity ringdown spectroscopy for sensitive and rapid molecular detection. Science **311**, 1595–1599 (2006)
80. R.A. Goldsby, *Immunology*, 5th edn. (W.H. Freeman, USA 2003)
81. J.R. Uzarski, C.M. Mello, Detection and classification of related lipopolysaccharides via a small array of immobilized antimicrobial peptides. Anal. Chem. **84**, 7359–7366 (2012)
82. T.Z. Wu, Y.R. Lo, E.C. Chan, Exploring the recognized bio-mimicry materials for gas sensing. Biosens. Bioelectron. **16**, 945–953 (2001)
83. M. Mascini, A. Macagnano, D. Monti, M. Del Carlo, R. Paolesse, B. Chen, P. Warner, A. D'Amico, C. Di Natale, D. Compagnone, Piezoelectric sensors for dioxins: a biomimetic approach. Biosens. Bioelectron. **20**, 1203–1210 (2004)
84. C. Buerger, K. Nagel-Wolfrum, C. Kunz, I. Wittig, K. Butz, F. Hoppe-Seyler, B. Groner, Sequence-specific peptide aptamers, interacting with the intracellular domain of the epidermal growth factor receptor, interfere with Stat3 activation and inhibit the growth of tumor cells. J. Biol. Chem. **278**, 37610–37621 (2003)
85. P. Colas, B. Cohen, T. Jessen, I. Grishina, J. McCoy, R. Brent, Genetic selection of peptide aptamers that recognize and inhibit cyclin-dependent kinase 2. Nature **380**, 548–550 (1996)
86. Y. Cui, S.N. Kim, R.R. Naik, M.C. McAlpine, Biomimetic peptide nanosensors. Acc. Chem. Res. **45**, 696–704 (2012)
87. M. Sarikaya, C. Tamerler, A.K. Jen, K. Schulten, F. Baneyx, Molecular biomimetics: nanotechnology through biology. Nat. Mater. **2**, 577–585 (2003)
88. R.R. Naik, S.J. Stringer, G. Agarwal, S.E. Jones, M.O. Stone, Biomimetic synthesis and patterning of silver nanoparticles. Nat. Mater. **1**, 169–172 (2002)
89. N. Bowden, A. Terfort, J. Carbeck, G.M. Whitesides, Self-assembly of mesoscale objects into ordered two-dimensional arrays. Science **276**, 233–235 (1997)
90. D. Kisailus, Q. Truong, Y. Amemiya, J.C. Weaver, D.E. Morse, Self-assembled bifunctional surface mimics an enzymatic and templating protein for the synthesis of a metal oxide semiconductor. Proc. Natl. Acad. Sci. USA. **103**, 5652–5657 (2006)
91. R.F Service. Can sensors make a home in the body? Science 297, 962–963 (2002)
92. H. Yao, A.J. Shum, M. Cowan, I. Lahdesmaki, B.A. Parviz, A contact lens with embedded sensor for monitoring tear glucose level. Biosens. Bioelectron. **26**, 3290–3296 (2011)
93. A.C.R. Grayson, R.S. Shawgo, A.M. Johnson, N.T. Flynn, Y. Li, M.J. Cima, R. Langer, A bioMEMS review: MEMS technology for physiologically integrated devices. Proc. IEEE. **92**, 6–21 (2004)
94. M.L. Neat, R. Peacock, R.T. Brittain, Implantation of electrodes in the dentine of an upper canine tooth in the dog. Br. J. Pharmacol. **43**, 476P–477P (1971)
95. C.M. Li, H. Dong, X. Cao, J.H. Luong, X. Zhang, Implantable electrochemical sensors for biomedical and clinical applications: progress, problems, and future possibilities. Curr. Med. Chem. **14**, 937–951 (2007)

96. M.O. Schurr, S. Schostek, C.N. Ho, F. Rieber, A. Menciassi, Microtechnologies in medicine: an overview. Minim. Invasiv. Ther. **16**, 76–86 (2007)
97. C. Vepari, D.L. Kaplan, Silk as a Biomaterial. Prog. Polym. Sci. **32**, 991–1007 (2007)
98. D.H. Kim, Y.S. Kim, J. Amsden, B. Panilaitis, D.L. Kaplan, F.G. Omenetto, M.R. Zakin, J.A. Rogers, Silicon electronics on silk as a path to bioresorbable, implantable devices. Appl. Phys. Lett. **95**, 133701 (2009)
99. K.G. Ong, C.A. Grimes, C.L. Robbins, R.S. Singh, Design and application of a wireless, passive, resonant-circuit environmental monitoring sensor. Sens. Actuators, A **93**, 33–43 (2001)
100. K.G. Ong, J. Wang, R.S. Singh, L.G. Bachas, C.A. Grimes, Monitoring of bacteria growth using a wireless, remote query resonant-circuit sensor: application to environmental sensing. Biosens. Bioelectron. **16**, 305–312 (2001)
101. A.C. Ferrari, J.C. Meyer, V. Scardaci, C. Casiraghi, M. Lazzeri, F. Mauri, S. Piscanec, D. Jiang, K.S. Novoselov, S. Roth, A.K. Geim, Raman spectrum of graphene and graphene layers. Phys. Rev. Lett. **97**, 187401 (2006)
102. J.A. Timlin, A. Carden, M.D. Morris, R.M. Rajachar, D.H. Kohn, Raman spectroscopic imaging markers for fatigue-related microdamage in bovine bone. Anal. Chem. **72**, 2229–2236 (2000)
103. U.B. Schaad, Which number of infecting bacteria is of clinical relevance? Infection **11**(Suppl 2), S87–89 (1983)
104. G.A. Zelada-Guillen, J. Riu, A. Duzgun, F.X. Rius, Immediate detection of living bacteria at ultralow concentrations using a carbon nanotube based potentiometrie aptasensor. Angew. Chem. Int. Ed. Engl. **48**, 7334–7337 (2009)
105. P. Belgrader, W. Benett, D. Hadley, J. Richards, P. Stratton, R. Mariella Jr., F. Milanovich, PCR detection of bacteria in seven minutes. Science **284**, 449–450 (1999)
106. Y. Li, Y.T. Cu, D. Luo, Multiplexed detection of pathogen DNA with DNA-based fluorescence nanobarcodes. Nat. Biotechnol. **23**, 885–889 (2005)
107. Y. Cui, S.N. Kim, S.E. Jones, L.L. Wissler, R.R. Naik, M.C. McAlpine, Chemical functionalization of graphene enabled by phage displayed peptides. Nano Lett. **10**, 4559–4565 (2010)
108. M.J. Pender, L.A. Sowards, J.D. Hartgerink, M.O. Stone, R.R. Naik, Peptide-mediated formation of single-wall carbon nanotube composites. Nano Lett. **6**, 40–44 (2006)
109. M. Zelzer, R.V. Ulijn, Next-generation peptide nanomaterials: molecular networks, interfaces and supramolecular functionality. Chem. Soc. Rev. **39**, 3351–3357 (2010)
110. M.S. Mannoor, S. Zhang, A.J. Link, M.C. McAlpine, Electrical detection of pathogenic bacteria via immobilized antimicrobial peptides. Proc. Natl. Acad. Sci. USA. **107**, 19207–19212 (2010)
111. N.V. Kulagina, K.M. Shaffer, G.P. Anderson, F.S. Ligler, C.R. Taitt, Antimicrobial peptide-based array for *Escherichia coli* and *Salmonella* screening. Anal. Chim. Acta. **575**, 9–15 (2006)
112. M. Zasloff, Antimicrobial peptides of multicellular organisms. Nature **415**, 389–395 (2002)
113. L. Chen, Y. Li, J. Li, X. Xu, R. Lai, Q. Zou, An antimicrobial peptide with antimicrobial activity against *Helicobacter pylori*. Peptides **28**, 1527–1531 (2007)
114. S.N. Kim, Z. Kuang, J.M. Slocik, S.E. Jones, Y. Cui, B.L. Farmer, M.C. McAlpine, R.R. Naik, Preferential binding of peptides to graphene edges and planes. J. Am. Chem. Soc. **133**, 14480–14483 (2011)
115. M.A. Beard-Pegler, E. Stubbs, A.M. Vickery, Observations on the resistance to drying of staphylococcal strains. J. Med. Microbiol. **26**, 251–255 (1988)
116. M.A. Beard-Pegler, A.M. Vickery, Lysogenicity of methicillin-resistant strains of *Staphylococcus aureus*. J. Med. Microbiol. **20**, 147–155 (1985)
117. R.A. Potyrailo, W.G. Morris, Multianalyte chemical identification and quantitation using a single radio frequency identification sensor. Anal. Chem. **79**, 45–51 (2007)
118. N. Strand, A. Bhushan, M. Schivo, N.J. Kenyon, C.E. Davis, Chemically polymerized polypyrrole for on-chip concentration of volatile breath metabolites. Sens. Actuators B **143**, 516–523 (2010)

119. M. Phillips, Method for the collection and assay of volatile organic compounds in breath. Anal. Biochem. **247**, 272–278 (1997)
120. S. Webb, Attacks on asthma. Nat. Biotechnol. **29**, 860–863 (2011)
121. R. Beasley, J. Crane, C.K. Lai, N. Pearce, Prevalence and etiology of asthma. J. Allergy Clin. Immunol. **105**, 466–472 (2000)
122. World Health Organization, *W. H. O. Global surveillance, prevention and control of chronic respiratory diseases: a comprehensive approach*. (World Health Organization, Switzerland, 2007)
123. S. Kazani, E. Israel, Update in Asthma. Am. J. Respir. Crit. Care Med. **184**, 291–296 (2011)
124. L.J. Akinbami, K.C. Schoendorf, Trends in childhood asthma: prevalence, health care utilization, and mortality. Pediatrics **110**, 315–322 (2002)
125. P.A. Eggleston, Environmental causes of asthma in inner city children. The national cooperative inner city asthma study. Clin. Rev. Allergy Immunol. **18**, 311–324 (2000)
126. H. Pinnock, R. Shah, Asthma. BMJ **334**, 847–850 (2007)
127. American Thoracic Society/European Respiratory Society (ATS/ERS) recommendations for standardized procedures for the online and offline measurement of exhaled lower respiratory nitric oxide and nasal nitric oxide, 2005. Am. J. Respir. Crit. Care Med. **171**, 912–930 (2005)
128. R.F. Lemanske, W.W. Busse, Asthma: clinical expression and molecular mechanisms. J. Allergy Clin. Immunol. **125**, 95–102 (2010)
129. F.D. Martinez, Development of wheezing disorders and asthma in preschool children. Pediatrics **109**, 362–367 (2002)
130. A.L. Lefkovitz, B.J. Zarowitz, Is that case of asthma really COPD, and does the diagnosis matter? Geriatr. Nur. (Lond.). **30**, 409–413 (2009)
131. P.J. Barnes, Immunology of asthma and chronic obstructive pulmonary disease. Nat. Rev. Immunol. **8**, 183–192 (2008)
132. S.T. Holgate, R. Polosa, Treatment strategies for allergy and asthma. Nat. Rev. Immunol. **8**, 218–230 (2008)
133. J.C. Renauld, New insights into the role of cytokines in asthma. J. Clin. Pathol. **54**, 577–589 (2001)
134. C.M. Robroeks, Q. Jobsis, J.G. Damoiseaux, P.H. Heijmans, P.P. Rosias, H.J. Hendriks, E. Dompeling, Cytokines in exhaled breath condensate of children with asthma and cystic fibrosis. Ann. Allergy Asthma. Immunol. **96**, 349–355 (2006)
135. C.M. Robroeks, G.T. Rijkers, Q. Jobsis, H.J. Hendriks, J.G. Damoiseaux, L.J. Zimmermann, O.P. van Schayck, E. Dompeling, Increased cytokines, chemokines and soluble adhesion molecules in exhaled breath condensate of asthmatic children. Clin. Exp. Allergy. **40**, 77–84 (2010)
136. T. Ichinose, K. Sadakane, H. Takano, R. Yanagisawa, M. Nishikawa, I. Mori, H. Kawazato, A. Yasuda, K. Hiyoshi, T. Shibamoto, Enhancement of mite allergen-induced eosinophil infiltration in the murine airway and local cytokine/chemokine expression by Asian sand dust. J. Toxicol. Environ. Health A **69**, 1571–1585 (2006)
137. S.K. Shahid, S.A. Kharitonov, N.M. Wilson, A. Bush, P.J. Barnes, Increased interleukin-4 and decreased interferon-gamma in exhaled breath condensate of children with asthma. Am. J. Respir. Crit. Care Med. **165**, 1290–1293 (2002)
138. W. Chen, Z. Lu, C.M. Li, Sensitive human interleukin 5 impedimetric sensor based on polypyrrole-pyrrolepropylic acid-gold nanocomposite. Anal. Chem. **80**, 8485–8492 (2008)
139. H.H.H. Shen, S.I. Ochkur, M.P. McGarry, J.R. Crosby, E.M. Hines, M.T. Borchers, H.Y. Wang, T.L. Biechelle, K.R. O'Neill, T.L. Ansay, D.C. Colbert, S.A. Cormier, J.P. Justice, N.A. Lee, J.J. Lee, A causative relationship exists between eosinophils and the development of allergic pulmonary pathologies in the mouse. J. Immunol. **170**, 3296–3305 (2003)
140. C.J. Sanderson, Interleukin-5, eosinophils, and disease. Blood **79**, 3101–3109 (1992)
141. K. Takatsu, A. Tominaga, N. Harada, S. Mita, M. Matsumoto, T. Takahashi, Y. Kikuchi, N. Yamaguchi, T cell-replacing factor (TRF)/interleukin 5 (IL-5): molecular and functional properties. Immunol. Rev. **102**, 107–135 (1988)

142. J. Hunt, Exhaled breath condensate: an evolving tool for noninvasive evaluation of lung disease. J. Allergy Clin. Immunol. **110**, 28–34 (2002)
143. G.M. Mutlu, K.W. Garey, R.A. Robbins, L.H. Danziger, I. Rubinstein, Collection and analysis of exhaled breath condensate in humans. Am. J. Respir. Crit. Care Med. **164**, 731–737 (2001)
144. A. Koch, J. Knobloch, C. Dammhayn, M. Raidl, A. Ruppert, H. Hag, D. Rottlaender, K. Muller, E. Erdmann, Effect of bacterial endotoxin LPS on expression of INF-gamma and IL-5 in T-lymphocytes from asthmatics. Clin. Immunol. **125**, 194–204 (2007)
145. L. Borg, J. Kristiansen, J.M. Christensen, K.F. Jepsen, L.K. Poulsen, Evaluation of accuracy and uncertainty of ELISA assays for the determination of interleukin-4, interleukin-5, interferon-gamma and tumor necrosis factor-alpha. Clin. Chem. Lab. Med. **40**, 509–519 (2002)
146. M. Tary-Lehmann, D.E. Hricik, A.C. Justice, N.S. Potter, P.S. Heeger, Enzyme-linked immunosorbent assay spot detection of interferon-gamma and interleukin 5-producing cells as a predictive marker for renal allograft failure. Transplantation **66**, 219–224 (1998)
147. R.M. Effros, R. Casaburi, J. Su, M. Dunning, J. Torday, J. Biller, R. Shaker, The effects of volatile salivary acids and bases on exhaled breath condensate pH. Am. J. Respir. Crit. Care Med. **173**, 386–392 (2006)
148. I. Horvath, J. Hunt, P.J. Barnes, K. Alving, A. Antczak, E. Baraldi, G. Becher, W.J. van Beurden, M. Corradi, R. Dekhuijzen, R.A. Dweik, T. Dwyer, R. Effros, S. Erzurum, B. Gaston, C. Gessner, A. Greening, L.P. Ho, J. Hohlfeld, Q. Jobsis, D. Laskowski, S. Loukides, D. Marlin, P. Montuschi, A.C. Olin, A.E. Redington, P. Reinhold, E.L. van Rensen, I. Rubinstein, P. Silkoff, K. Toren, G. Vass, C. Vogelberg, H. Wirtz, Exhaled breath condensate: methodological recommendations and unresolved questions. Eur. Respir. J. **26**, 523–548 (2005)
149. K.S. Novoselov, D. Jiang, F. Schedin, T.J. Booth, V.V. Khotkevich, S.V. Morozov, A.K. Geim, Two-dimensional atomic crystals. Proc. Natl. Acad. Sci. USA. **102**, 10451–10453 (2005)
150. E.D. Minot, A.M. Janssens, I. Heller, H.A. Heering, C. Dekker, S.G. Lemay, Carbon nanotube biosensors: the critical role of the reference electrode. Appl. Phys. Lett. **91**, 093507 (2007)
151. T. Lohmann, K. von Klitzing, J.H. Smet, Four-terminal magneto-transport in graphene p-n junctions created by spatially selective doping. Nano Lett. **9**, 1973–1979 (2009)
152. F. Schwierz, Graphene transistors. Nat. Nanotech. **5**, 487–496 (2010)
153. A. Pirkle, J. Chan, A. Venugopal, D. Hinojos, C.W. Magnuson, S. McDonnell, L. Colombo, E.M. Vogel, R.S. Ruoff, R.M. Wallace, The effect of chemical residues on the physical and electrical properties of chemical vapor deposited graphene transferred to SiO_2. Appl. Phys. Lett. **99**, 122108 (2011)
154. M.Y. Yeh, E.L. Burnham, M. Moss, L.A. Brown, Non-invasive evaluation of pulmonary glutathione in the exhaled breath condensate of otherwise healthy alcoholics. Respir. Med. **102**, 248–255 (2008)
155. T. Ueno, M. Kataoka, A. Hirano, K. Iio, Y. Tanimoto, A. Kanehiro, C. Okada, R. Soda, K. Takahashi, M. Tanimoto, Inflammatory markers in exhaled breath condensate from patients with asthma. Respirology **13**, 654–663 (2008)
156. J.N. Israelachvili, *Intermolecular and Surface Forces*, 3rd edn. (Academic, USA 2011)
157. E. Stern, R. Wagner, F.J. Sigworth, R. Breaker, T.M. Fahmy, M.A. Reed, Importance of the Debye screening length on nanowire field effect transistor sensors. Nano Lett. **7**, 3405–3409 (2007)
158. S. Sorgenfrei, C.Y. Chiu, M. Johnston, C. Nuckolls, K.L. Shepard, Debye screening in single-molecule carbon nanotube field-effect sensors. Nano Lett. **11**, 3739–3743 (2011)
159. R.J. Chen, Y. Zhang, D. Wang, H. Dai, Noncovalent sidewall functionalization of single-walled carbon nanotubes for protein immobilization. J. Am. Chem. Soc. **123**, 3838–3839 (2001)

160. D.W. Boukhvalov, M.I. Katsnelson, Chemical functionalization of graphene with defects. Nano Lett. **8**, 4373–4379 (2008)
161. P.R. Nair, M.A. Alam, Screening-limited response of nanobiosensors. Nano Lett. **8**, 1281–1285 (2008)
162. K. Cung, R.L. Slater, Y. Cui, S.E. Jones, H. Ahmad, R.R. Naik, M.C. McAlpine, Rapid, multiplexed microfluidic phage display. Lab Chip. **12**, 562–565 (2012)
163. L. Clifton, D.A. Clifton, M.A.F. Pimentel, P.J. Watkinson, L. Tarassenko, Predictive monitoring of mobile patients by combining clinical observations with data from wearable sensors. IEEE J. Biomed. Health. **18**, 722–730 (2014)

Chapter 10
Functionalized Carbon Nanodots for Biomedical Applications

Yun Kyung Jung, Yuri Choi and Byeong-Su Kim

10.1 Introduction

The use of biological labels has greatly assisted the study of complex biochemical interactions and the monitoring of their localization during disease diagnosis and therapy. Fluorescent labeling using organic fluorophores, genetically encoded fluorescent proteins, and semiconducting quantum dots (QDs) has been demonstrated as an indispensable tool for both in vivo and in vitro cellular imaging [1–5]. In contrast to the conventional organic dyes and the fluorescent proteins showing several deficiencies like broad-spectrum profiles, very short excited-state lifetimes, and their sensitivity to photobleaching, QDs have been intensively studied as a promising luminescent probe due to high resistance to photobleaching, large stokes shift, narrow size-dependent emission spectra, broad excitation spectra, and long fluorescence lifetime [1–5]. In addition, they have been engineered to carry therapeutic agents for simultaneous diagnosis and therapy (theranostics). Despite these notable advantages, the implementation of QDs to a broader clinical setting is still limited because of their intrinsic toxicity and the potential environmental concerns associated with the heavy metals present in the QDs.

In an attempt to develop benign alternatives, new kinds of nanoparticles with combined properties of carbon-based materials and QDs, such as graphene QDs (GQDs)[6–12] and carbon nanodots (also known as C-dots, carbon dots (CDs)) [12–25], have emerged. The GQDs, which are small graphene fragments with diameters below 30 nm, are fabricated by fragmentation or cutting from graphene oxide, and they have been used to deliver drugs to cells. However, because their fluorescence intensity is weak, and their emission wavelength often overlaps with cellular autofluorescence [8], the GQDs have limited application for biolabels.

Another carbon nanoparticle, the CD has emerged as a promising class of biolabels by virtue of their biocompatibility, low toxicity, tunable photoluminescence,

B.-S. Kim (✉) · Y. K. Jung
Department of Chemistry, School of Natural Science, Ulsan, Republic of Korea
e-mail: bskim19@unist.ac.kr

Y. Choi · B.-S. Kim
Department of Energy Engineering, School of Energy and Chemical Engineering, UNIST, Ulsan 689-798, Republic of Korea

M. Zhang et al. (eds.), *Carbon Nanomaterials for Biomedical Applications,*
Springer Series in Biomaterials Science and Engineering 5,
DOI 10.1007/978-3-319-22861-7_10

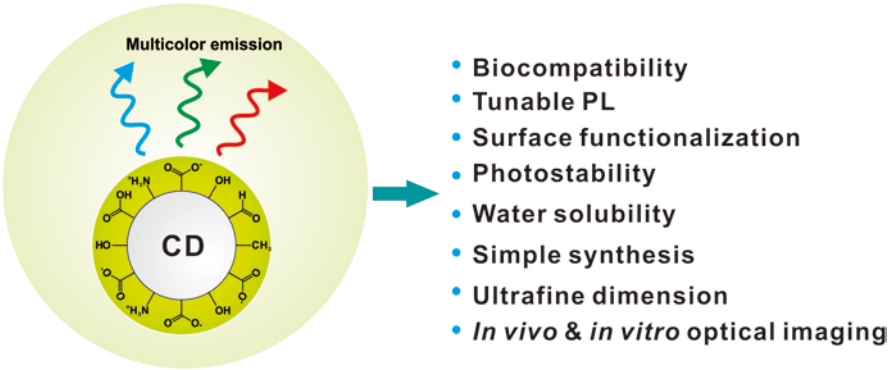

Fig. 10.1 Advantages of carbon dots (CDs) for optical imaging and drug delivery

high chemical/photostability, and mass production by a simple preparation method, while retaining the advantageous photophysical features of QDs (Fig. 10.1) [12–16]. The fluorescence emission spectra of CDs exhibited an excitation-dependent feature, which is quite different from that of QDs and organic dyes, enabling multicolor fluorescence detection for in vitro optical imaging [17–19]. Furthermore, the CDs are generally composed of a mixed phase of sp^2- and sp^3-hybridized carbon nanostructures in the form of conjugated carbon clusters functionalized with oxygen-bearing functional groups [17]. Aside the strong fluorescence of CDs, their unique chemical structure allows the integration of active therapeutic molecules into the sp^2 carbon frame via strong π–π interactions, and their surface functional groups enable further conjugation with other molecules such as biological affinity ligands. These unique characteristics make CDs ideal drug carriers, which lead to advances in personalized medicine [20–25]. Therefore, in this chapter, the application of the CDs for photodynamic therapy (PDT) and chemotherapy is discussed, and enhanced therapeutic efficacy of drugs by CD-aided delivery is evaluated in vitro and in vivo.

10.2 CD-Based Photodynamic Therapy for Cancer In Vitro and In Vivo

Due to high fluorescence and photostability, CDs have gained attention as biolabeling materials [16]. Also, with sp^2 carbon structure and the abundant functional groups, CDs can be easily functionalized with biological affinity ligands and act as drug carriers in aqueous solution [17].

Recently, as photosensitizer (PS) carrier for PDT, highly biocompatible and fluorescent CDs were developed (Fig. 10.2) [21]. With oxygen functional groups, the

surface of the CD was subsequently passivated with poly(ethylene glycol) diamine (PEG) and folic acid (FA) to enhance its fluorescence as well as increase the affinity for cancerous cells [21, 26]. As a second-generation PS, zinc phthalocyanine (ZnPc) possesses good cytotoxic efficiency. This carbon nanomaterial (CD–PEG–FA) has dual ability, which is simultaneous biological imaging and targeted PDT in vitro and in vivo.

In fluorescence spectrum, the fluorescence emission maxima of CD–PEG–FA were located at 450 nm and excited at 360 nm (Fig. 10.3a). Also, 10.9 % of quantum yield and 5.52 ns of the exciton lifetime were calculated. The broad UV/vis absorption represented the successful functionalization of FA onto the CD surface from the peak at 283 nm, and CD–PEG–FA displayed bright blue emission under UV irradiation (Fig. 10.3b). Furthermore, Fourier-transform infrared (FT-IR) spectroscopy revealed changes in the chemical functional groups on the CDs upon surface passivation. After passivation with PEG and FA, CD–PEG–FA exhibited characteristic peaks at the peak 1102 cm^{-1} from C–O groups of PEG and 1481, 1605, and 1697 cm^{-1} which corresponded to FA (Fig. 10.3c) [27]. The transmission electron microscopy (TEM) images showed a spherical morphology of the CDs with an average diameter of 4.5 ± 0.2 nm for CD–PEG–FA (Fig. 10.3d). The interlayer spacing of 0.34 nm, observed using high-resolution TEM, corresponded to that of graphitic carbon, representing the graphitic nature of the CDs. For photodynamic therapy, CD–PEG–FA/ZnPc composite was synthesized via π-π stacking interaction, which had 60 μg of ZnPc per milligram of CD–PEG–FA (Fig. 10.3e).

To confirm the efficacy of CD–PEG–FA and CD–PEG–FA/ZnPc in targeted bioimaging, the targeting of CDs was evaluated after incubation with the HeLa cells for 12 h, by monitoring the blue and red fluorescence of CD ($\lambda_{ex}/\lambda_{em}$ = 358/461 nm) and ZnPc ($\lambda_{ex}/\lambda_{em}$ = 647/665 nm), respectively (Fig. 10.4). As a result, the cells incubated with CD–PEG–FA displayed intense CD fluorescence in the cytoplasm, and CD–PEG–FA/ZnPc showed prominent fluorescence signals of both the blue (CD) and red (ZnPc) channels, indicating the successful intracellular delivery of ZnPc by the CD carrier. To clarify the targeting role of FA, a competition assay was performed with free FA, which resulted to no cellular internalization. This result indicated that CD–PEG–FA successfully targeted to cancer cell.

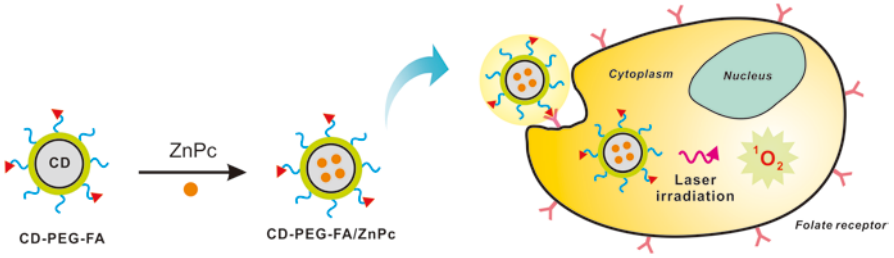

Fig. 10.2 Schematic illustration of targeted PDT with folic-acid-functionalized carbon nanodots loaded with zinc phthalocyanine (CD–PEG–FA/ZnPc)

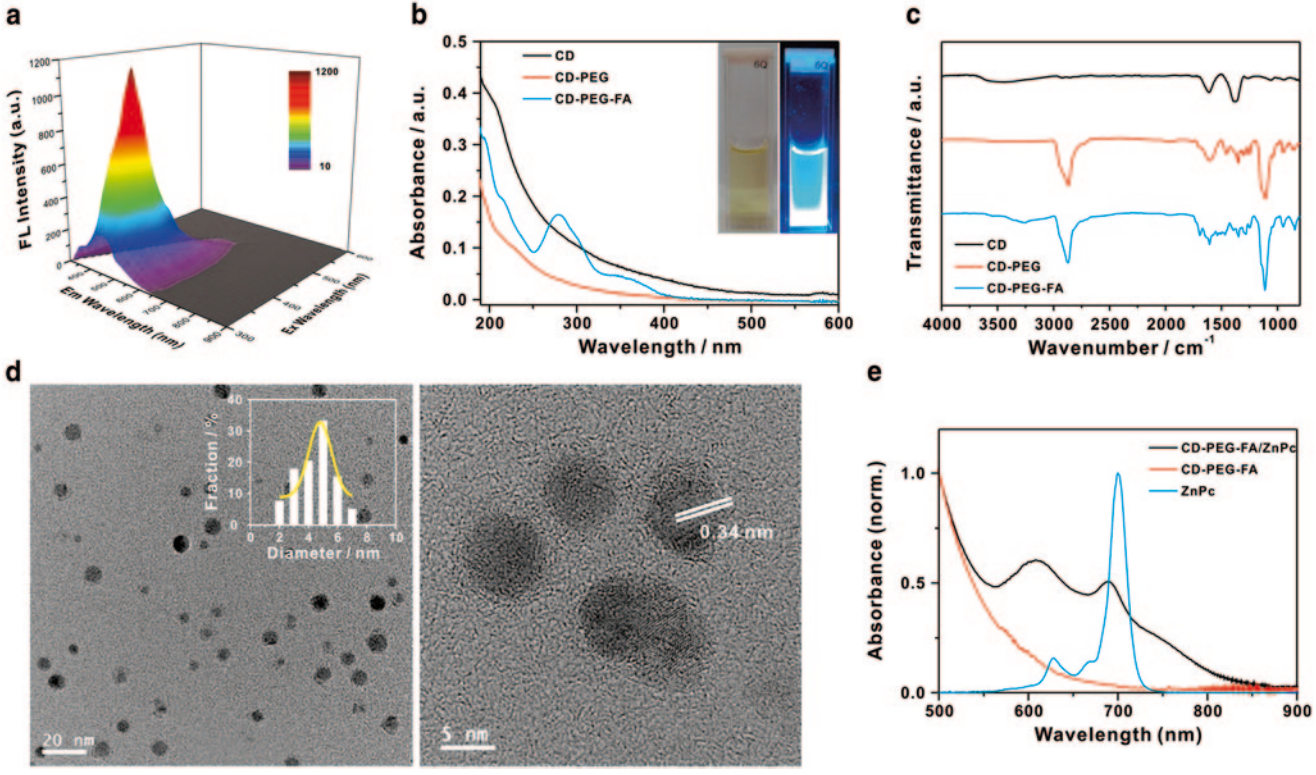

Fig. 10.3 **a** Three-dimensional fluorescence spectra of CD–PEG–FA under varying excitation wavelengths from 300 to 600 nm with 10-nm increments. **b** UV–vis absorbance spectra of CD, CD–PEG, and CD–PEG–FA. **c** FT-IR spectra of CD, CD–PEG, and CD–PEG–FA. **d** TEM images of CD–PEG–FA with a corresponding size distribution histogram. Inset shows the CD–PEG–FA suspension *(left)* under room light and *(right)* UV illumination at 365 nm. **e** UV–vis absorbance spectra of *(red)* CD–PEG–FA, *(black)* CD–PEG–FA/ZnPc, and *(blue)* free ZnPc.

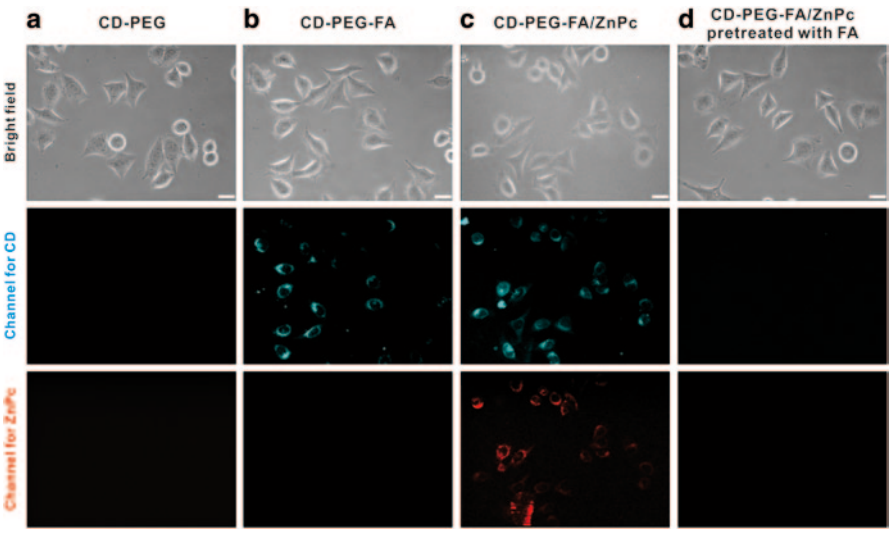

Fig. 10.4 (**a**–**d**) Bright-field and fluorescence images of HeLa cells treated with CD derivatives (50 μg/ml) for 12 h. **a** CD–PEG, **b** CD–PEG–FA, **c** CD–PEG–FA/ZnPc, and **d** CD–PEG–FA/ZnPc pretreated with FA. Fluorescence signals of *(blue)* CDs and *(red)* ZnPc were observed at 461 (λ_{ex} = 358 nm) and 665 nm (λ_{ex} = 647 nm), respectively. Scale bar is 20 μm

PDT was performed on the HeLa cells with the CD derivatives. CD–PEG–FA/ZnPc exhibited excellent PDT efficiency with significant cell death, whereas other samples treated with CD–PEG, CD–PEG–FA and FA-pretreated CD–PEG–FA/ZnPc did not exhibit measurable photodynamic activity (Fig. 10.5a–d).

In addition, the generation of the active singlet oxygen species via photoinduced energy transfer from ZnPc was quantified by using the singlet oxygen sensor green (SOSG) reagent, which reacts with singlet oxygen generated from the PS [28, 29]. Figure 10.6a showed the fluorescence intensity as a function of irradiation time; the intensity gradually increased upon irradiation with a light-emitting diode (LED; 30 mW/cm^2). While the control ZnPc without SOSG did not exhibit any fluorescence changes, ZnPc and CD–PEG–FA/ZnPc mixed with SOSG showed an increase in the fluorescence intensity upon irradiation. Because of intermolecular energy transfer between ZnPc and CD, the CD–PEG–FA/ZnPc did not effectively generate singlet oxygen relative to free ZnPc with SOSG. However, singlet oxygen generation was considerably accelerated upon the addition of cell lysate (Fig. 10.6a, t = 25 min), indicating the release of ZnPc from CD via the competitive displacement of ZnPc by interaction with the biomolecules in cell lysate, thus enhancing the therapeutic efficiency of PDT (Fig. 10.6b).

Encouraged by the high PDT efficacy in vitro, the PDT efficacy of the CD-mediated PS delivery system in animal models was investigated. As shown in Fig. 10.7a, b, the mice treated with CD–PEG–FA/ZnPc showed strong fluorescence signals

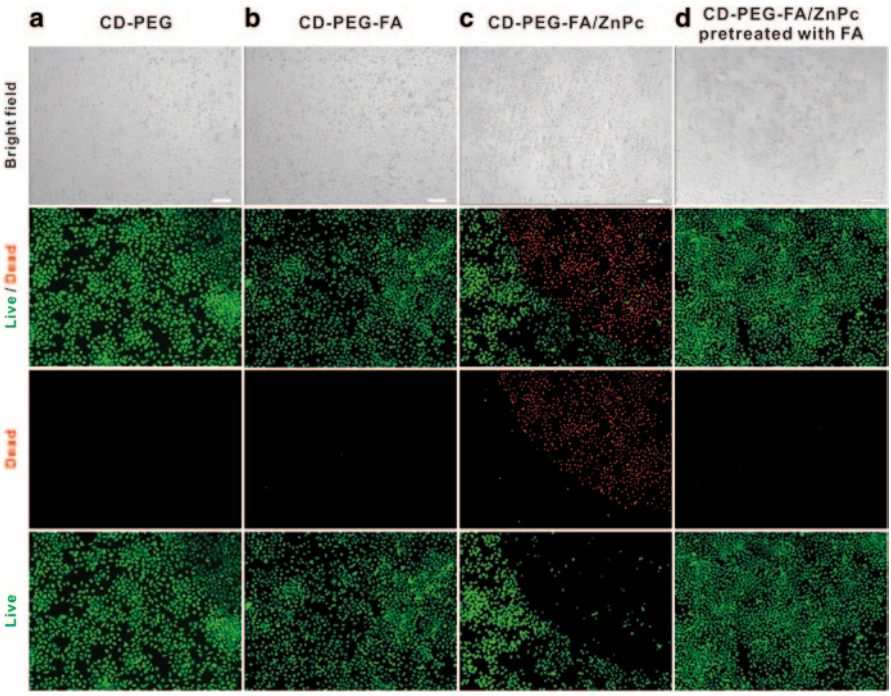

Fig. 10.5 (**a**–**d**; *top* panel) Bright-field and fluorescence images of HeLa cells treated with CD derivatives (50 μg/ml) for 12 h, followed by irradiation for 10 min with a 660-nm laser (30 mW/cm^2), and (*bottom* panels) live and dead cells colored *green* and *red,* respectively, by live/dead assay. **a** CD–PEG, **b** CD–PEG–FA, **c** CD–PEG–FA/ZnPc, and **d** CD–PEG–FA/ZnPc with pretreatment of excess free FA. Scale bar is 100 μm

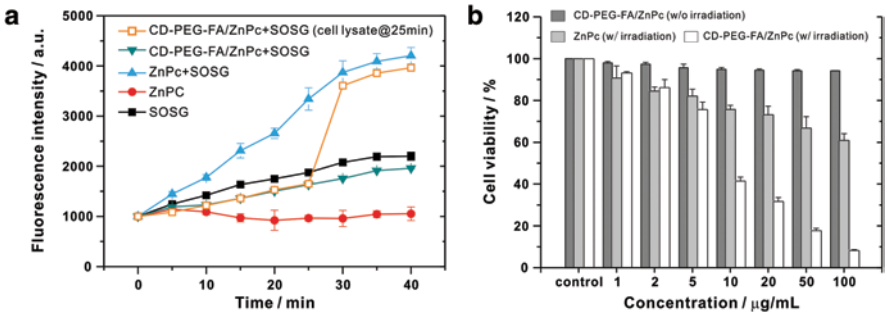

Fig. 10.6 Quantitative evaluation of photodynamic effect. **a** Singlet oxygen detection test using an SOSG reagent. Time-dependent fluorescent intensity ($\lambda_{ex}/\lambda_{em}$ = 504/530 nm) with irradiation by using a 660-nm laser (30 mW/cm^2). **b** Cell viability assay depending on the concentration of ZnPc-loaded CD–PEG–FA and ZnPc with and without irradiation for 10 min

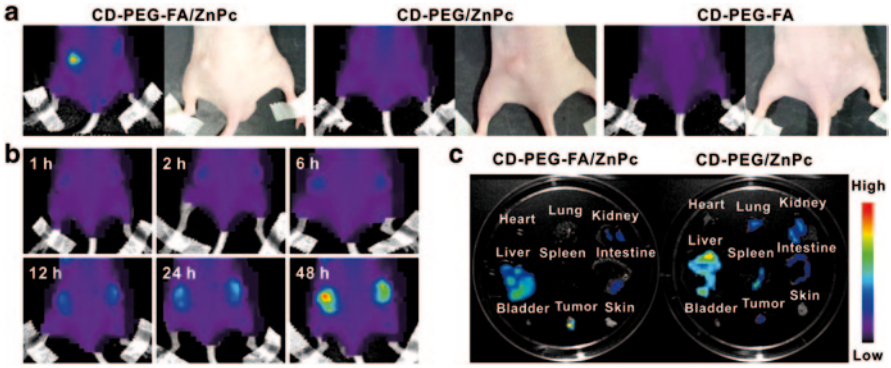

Fig. 10.7 **a** Fluorescence of ZnPc (excited at 660 nm) in tumor was imaged after a 12-h injection of CD–PEG–FA/ZnPc, CD–PEG/ZnPc, and CD–PEG–FA (0.5 mg of ZnPc/kg mouse). **b** CD–PEG–FA/ZnPc suspensions were injected into tail veins of tumor-bearing mice, and the fluorescent signals were obtained at various time points (1, 2, 6, 12, 24, and 48 h). **c** Ex vivo fluorescence images of major organs of mice. The fluorescent signals corresponding to ZnPc (excited at 660 nm) from major organs, tumor, and skin were obtained after 12 h of IV injection of CD–PEG–FA/ZnPc and CD–PEG/ZnPc into tumor-bearing mice. FA-conjugated CD delivered and released ZnPc to tumor effectively, in contrast with the CD lacking FA

corresponding to ZnPc in tumors, with gradual increase in the fluorescence intensity over time, in contrast to the mice treated with CD–PEG/ZnPc or CD–PEG–FA. Fluorescence images of the major organs in Fig. 10.7c showed that the fluorescence corresponding ZnPc were intense in liver and spleen rather than tumor in case of the mouse injected with CD–PEG/ZnPc, suggesting that most of the CDs omitting targeting ligand FA leaked out by circulation and prominently accumulated in reticuloendothelial system of the liver and spleen [30, 31]. These results showed that conjugation of FA to CD played an important role in greatly improving the active tumor-targeting capability of the ZnPc delivery vehicle to folate receptor-overexpressing tumors.

Finally, to investigate the therapeutic efficacy in vivo, changes in tumor volumes were monitored for 10 days after CD–PEG–FA, CD–PEG/ZnPc, and CD–PEG–FA/ZnPc (0.5 mg of ZnPc/kg of mouse) were intravenously injected to mice whose tumor volumes were ~70 mm^3 (Fig. 10.8). After irradiation with a 660-nm laser (0.3 W/cm^2, 20 min), the mice treated with CD–PEG–FA/ZnPc showed remarkable suppression of tumor growth as compared to the control mice for 8 days. However, the mice treated with CD–PEG/ZnPc and CD–PEG–FA, with or without laser irradiation, showed no notable difference in tumor size compared to the controls. Collectively, the in vivo study suggested that the present tumor-targeted CD-based PDT therapeutic agent delivery system can effectively induce the accumulation of the PS-loaded CDs in tumors, thus leading to enhanced therapeutic efficacy with a relatively small quantity of ZnPc.

In conclusion, CD–PEG–FA successfully demonstrated the targeted delivery of a PS via FA-mediated endocytosis of biocompatible CD–PEG–FA/ZnPc and

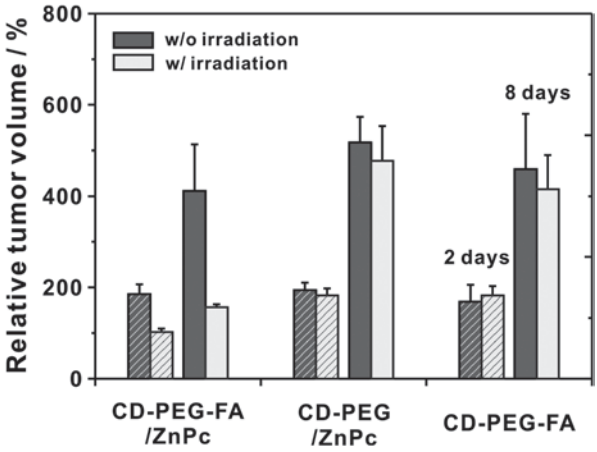

Fig. 10.8 Relative tumor volumes measured over time after the tumor-bearing mice were treated with various CD derivatives

therapeutic photodynamic efficacy by singlet oxygen generation from the internalized ZnPc upon light irradiation in vitro and in vivo. We anticipate that the present CD-based targeted delivery of the PS would offer a convenient and effective platform for enhanced PDT to treat cancers in the near future because of its excellent biocompatibility, bioimaging and targeting capability, and therapeutic efficacy.

10.3 Zwitterionic CD-Based Drug Delivery for Chemotherapy In Vitro and In Vivo

Nuclear-targeting drug-delivery systems (DDSs) have attracted significant attention in the biomedical applications, because they substantially increase the healing efficiency especially for tumor therapy [32–34]. Since many anticancer drugs are required to enter the cell nucleus where the drugs damage the genes to stop proliferation of the cancer cell, the construction of the nuclear-targeting DDSs is crucial to treat the tumors. Typically, for nuclear targeting, carriers need to be functionalized with the proper ligands such as nuclear localization signaling (NLS) peptides (nuclear membrane-penetrating peptides) on the surface [32–34]. Moreover, since the carriers cannot be acted as a fluorescent imaging probe, it should be conjugated with an organic fluorescent dye for tracking the individual drug-delivery event.

The highly luminescent CDs have emerged as a prospective class of biolabels by virtue of their tunable photoluminescence, biocompatibility, low toxicity, and mass production by a simple preparation method [12–25]. Furthermore, the CDs contain an sp^2- and sp^3-hybridized carbon structure that can load aromatic drugs via strong π–π interactions, making them a promising drug carrier for disease treatment. However, most CDs reported to date are localized to the cell cytoplasm, including the lysosomes, mitochondria, Golgi apparatus, and endoplasmic reticulum [12–25]. Therefore, it is evident that the next step in the evolution of CD is enabling it to reach the cell nucleus without being trapped in the cell cytoplasm.

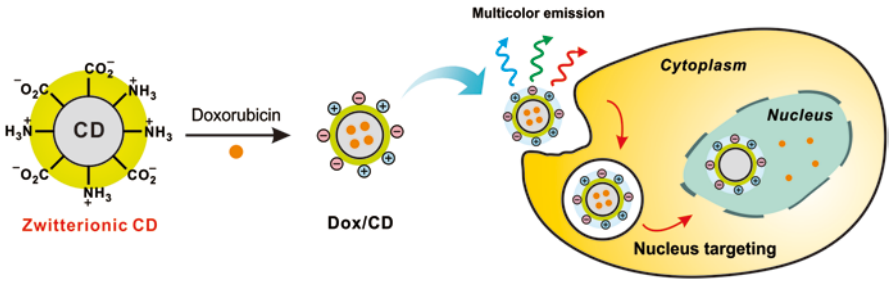

Fig. 10.9 Schematic illustration of the fabrication of doxorubicin-loaded carbon dot (*Dox/CD*), and simultaneous cell imaging and efficient Dox delivery to the nucleus by the zwitterionic *CD* vehicle

Cytoplasmic and nuclear uptake of nanoparticle cargo in live cells can be determined by the size [35] and surface charge [36–39]. In addition, positively charged nanoparticles are preferentially internalized by cells and negatively charged ones interact with nuclei whose pH is consistently 0.3–0.5 units above that of the cytosol [36–39]. Based on this observation, it is expected that the preparation of zwitterionic CDs, with both positively and negatively charged functional groups, can facilitate cytoplasmic uptake and subsequent nuclear translocation of theranostic drug–vehicle conjugates [40–45].

Multifunctional zwitterionic CDs have been fabricated via a simple one-pot synthesis using citric acid (CA) as a carbon source and an amino acid derivative, β-alanine (β-Ala), as a zwitterionic passivating agent, thus avoiding complexity and safety concerns. In vitro study has shown that the synthesized CDs were delivered into cell nuclei by their multicolor fluorescence. Furthermore, the CD-based DDS constructed by the non-covalent grafting of anticancer drug doxorubicin (Dox) not only efficiently accelerated nuclear and tumor accumulation of Dox but also markedly enhanced the cytotoxicity in cancer both in vitro and in vivo, which is superior to many other nanoparticle-based Dox delivery systems (Fig. 10.9).

Zwitterionic CDs with 21.9% of quantum yield showed two characteristic absorption peaks at 248 and 335 nm, which is suggestive of an sp^2 carbon network[19, 21] and the n–π* transition of the carbonyl group [19, 24], respectively (Fig. 10.10a). A bright blue fluorescence under UV light with a maximum emission wavelength at 418 nm was observed upon excitation at 335 nm. Bulk production by a simple manufacturing process is another advantage of CDs over other QDs and GQDs, yielding over a gram-scale powder in a highly efficient manner (average isolated yield over 30%, inset in Fig. 10.10a). The CDs exhibited superior stability in aqueous solution, with a nearly neutral ς-potential (−5.09 ± 6.47 mV) at pH 7, due to the presence of the zwitterionic β-Ala, which has both negatively charged carboxylic acid and positively charged amine moieties. The surface charge of the CDs gradually increased from −44.1 ± 1.63 to 7.73 ± 1.43 mV with a decrease in pH from 11 to 3 (Fig. 10.10b).

FT-IR spectroscopy exhibited that the as-prepared CDs showed peaks at 1174 (C–O stretching), 1772 (C = O stretching), 2947 (C–H stretching), 1708, and

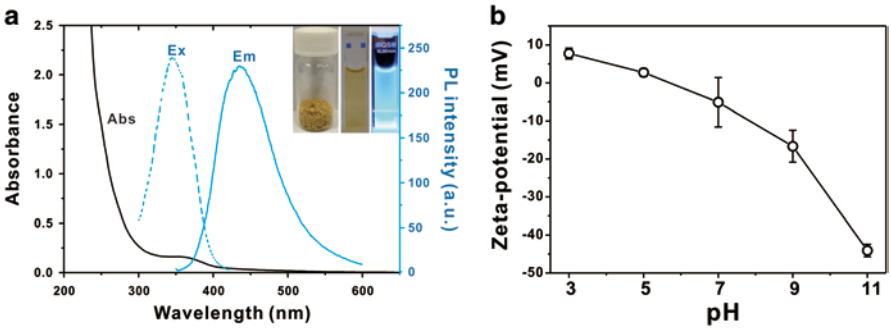

Fig. 10.10 **a** UV–vis absorbance, fluorescence excitation (λ_{em} = 435 nm) and emission (λ_{ex} = 340 nm) spectra of the CDs. Inset shows photographs of the CD powder (*left*), suspension under white light (*middle*), and suspension under UV light at 365 nm (*right*). **b** ς-potential of CDs with respect to pH

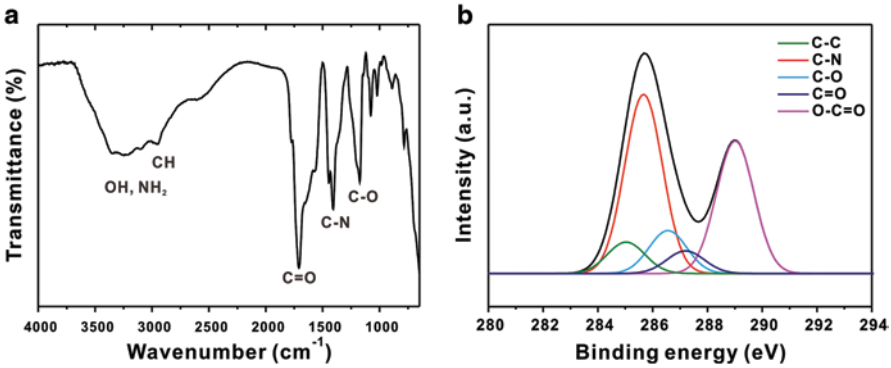

Fig. 10.11 **a** FT-IR spectrum and **b** deconvoluted high-resolution XPS C1s spectra of CD

1616 (the asymmetric and symmetric stretching vibrations of the carboxylate groups (COO^-)), and a broad peak around 3317 cm^{-1} (O–H and N–H stretching; Fig. 10.11a). The successful passivation of β-Ala was confirmed by the presence of amide bond bands at 3095 (N–H stretching) and 1409 cm^{-1} (C–N stretching). High-resolution X-ray photoelectron spectroscopy (XPS) spectra of the CDs further confirmed the successful surface passivation which indicates C–C (285.0 eV), C–N (285.7 eV), C–O (286.6 eV), C = O (287.2 eV), and O–C = O (289.0 eV) groups within CDs (Fig. 10.11b).

Figure 10.12a shows a high-resolution TEM (HRTEM) image of the CDs, revealing that the CDs had spherical shape with an average diameter of 3.09 ± 0.51 nm. In addition, aberration-corrected HRTEM allows to observe the hexagonal unit cells and a crystalline structure with an interlayer spacing of 0.24 nm (Fig. 10.12b), which corresponds to (111) lattice spacing of the graphite hexagons as confirmed by the fast Fourier transform (FFT) profile of a single CD (inset of Fig. 10.12b) [6, 10, 11].

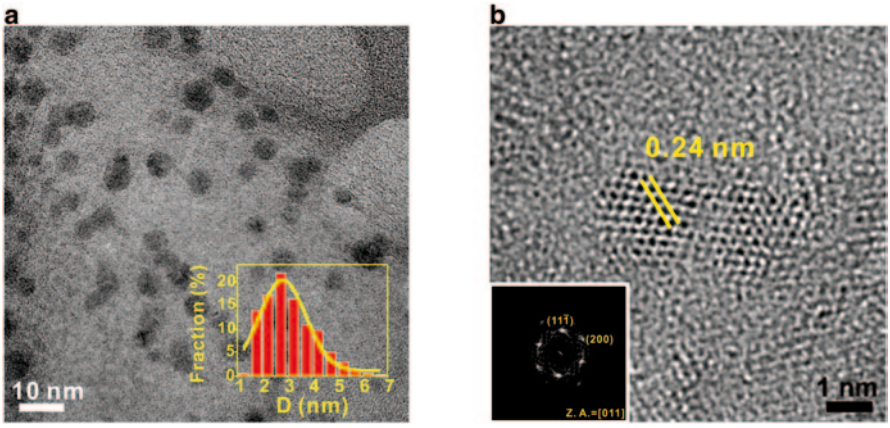

Fig. 10.12 **a**. TEM image of CDs with a corresponding size distribution histogram. **b** High-resolution TEM image showing the arrangement of carbon atoms in CDs with a lattice spacing of 0.24 nm. Inset is the corresponding *FFT* profile of a CD

The fluorescence emission spectra of CDs exhibited an excitation-dependent feature, which is quite different from that of QDs and organic dyes, enabling multicolor fluorescence detection. To evaluate the intracellular uptake and nuclear transport of the CD vehicles, the time-dependent localization of the CDs was studied after incubation with the human cervical cancer cell line, HeLa, for varying lengths of time by monitoring the blue, green, and red multicolor fluorescence signals of CD itself as well as by quantitatively measuring the fluorescence intensity within the cells (Fig. 10.13). The fluorescence of CDs began to appear in the cytoplasm after a 2-h treatment, suggesting that the CDs permeated the cell membrane. After a 6-h incubation, the CDs proceeded to move into the nucleus, a partially delocalized fluorescent signal was observed at the perinuclear region, and similar levels of fluorescence were monitored on both sides. Noticeably, significantly strong fluorescence of the cells after longer incubation periods (24 and 48 h) originates mainly from the nuclei.

The Bio-TEM images further demonstrated the clear nuclear localization of the CDs, in agreement with the strong fluorescence signals appeared in the nucleus after a 24-h incubation (Fig. 10.14). It should be noted that, although the CDs were not modified with any nuclear-targeted signals or chemicals, the CDs were successfully internalized into the cells as well as the nucleus which is attributed to the zwitterionic surface state and small size of CDs.

To use the CDs as a potential drug-delivery vehicle, the cytotoxicity of the CDs was evaluated in normal human WI-38 cells and cancer HeLa cells by 3-(4,5-dimethylthiazol-2-yl)-2,5-diphenyltetrazolium bromide (MTT) assay. The CDs were incubated for 24 h in a dose-dependent manner (10–1000 μg/mL) in triplicate. The CDs displayed remarkably low cytotoxicity (Fig. 10.15), with greater than 95 % cell viability at concentrations up to 500 μg/mL in both cell lines. These results indicate that the CDs are safe as a potential carrier for drug delivery.

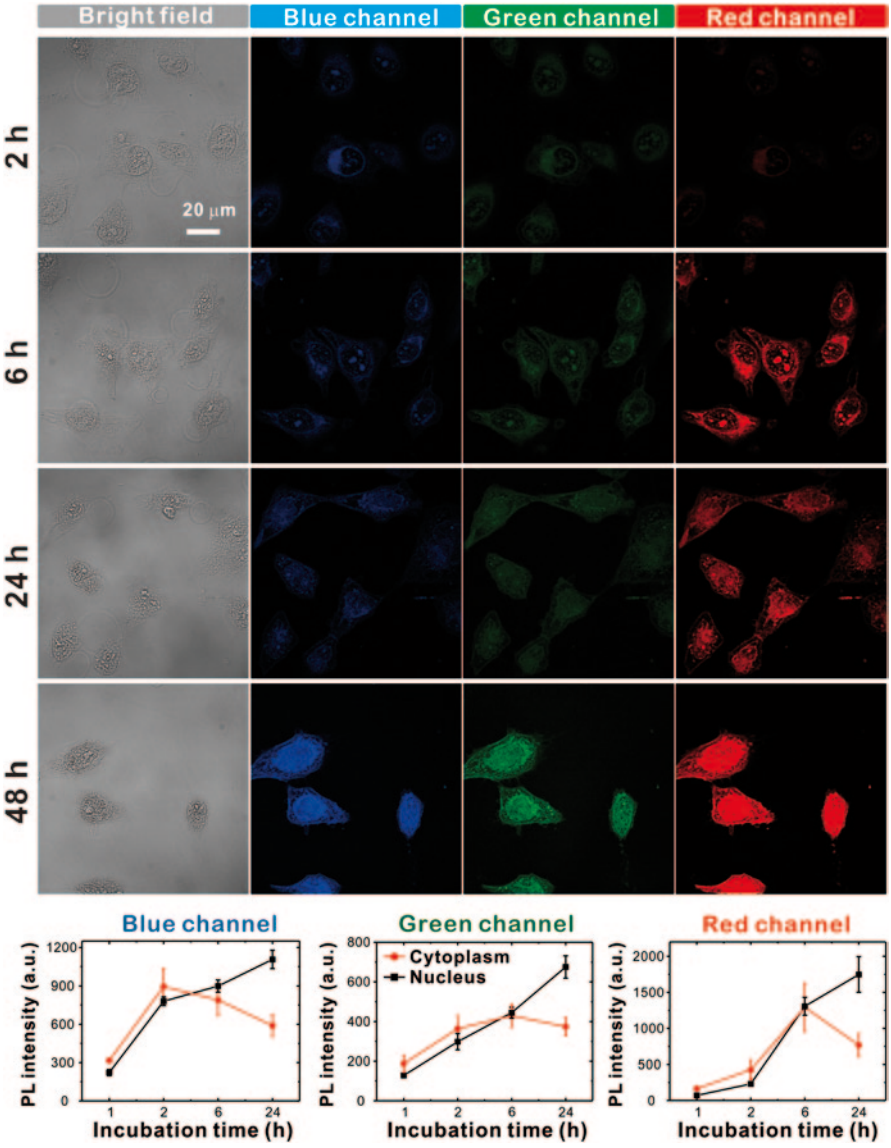

Fig. 10.13 Confocal fluorescence microscopy images showing the cytoplasmic and nuclear transport of CDs in HeLa cells. After treatment with 500 μg/mL CDs for varying amount of time, the *blue, green,* and *red* fluorescence signals of the CDs were observed under ultraviolet (405 nm), *blue* (473 nm), and *green* (559 nm) laser excitations, respectively. The fluorescence intensity in the nucleus and cytoplasm is measured separately and plotted in a time-dependent manner for each channel

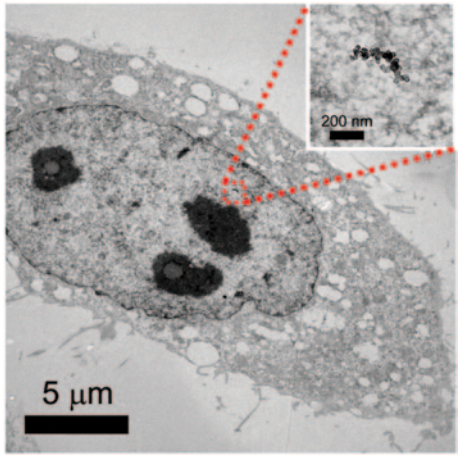

Fig. 10.14 Bio-TEM image of HeLa cells shows nuclear localization of CD. Inset is a zoom-in image of the *red* box in the main image

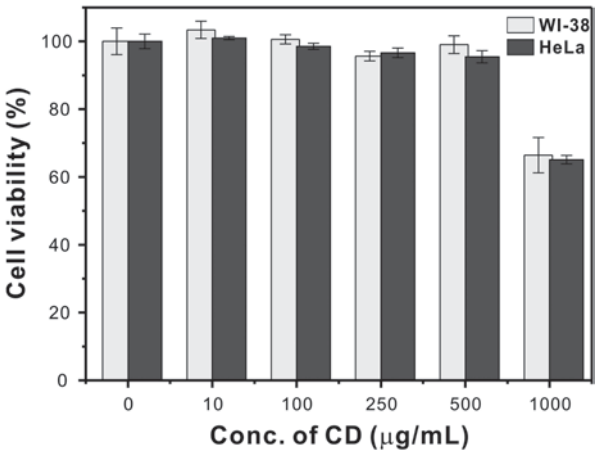

Fig. 10.15 Cell viability of WI-38 and HeLa cells treated with various CD concentrations for 24 h

The well-known anticancer chemotherapeutic drug Doxorubicin (Dox) has been widely used to treat a range of cancers, including cervical, gastric, and lung cancer, because it can directly intercalate with DNA to kill cancer cells [46]. However, when Dox is administered directly without a carrier, it displays low antitumor activity, due to lack of efficiency in reaching the nucleus. The CD-based drug-delivery vehicle was constructed by the non-covalent grafting of the anticancer drug Dox via strong π–π staking interactions between the sp^2-carbon network of CDs and the aromatic structure of Dox [12, 22–24]. The successful loading of Dox onto the CD was evident from the peaks at 339 and 474 nm, arising from respective CD and Dox, resulting in a loading of 14 wt% Dox in the CDs (Fig. 10.16a). Importantly, the ς-potential of the Dox/CD complex remained around zero (−5.92 ± 1.20 mV) at pH 7.0, indicating that the zwitterionic properties were preserved. The anticancer efficacy of Dox was evaluated by treating the HeLa cells with varying Dox or Dox/CD concentrations for 24 h. The HeLa cell viability clearly demonstrated that Dox/CD

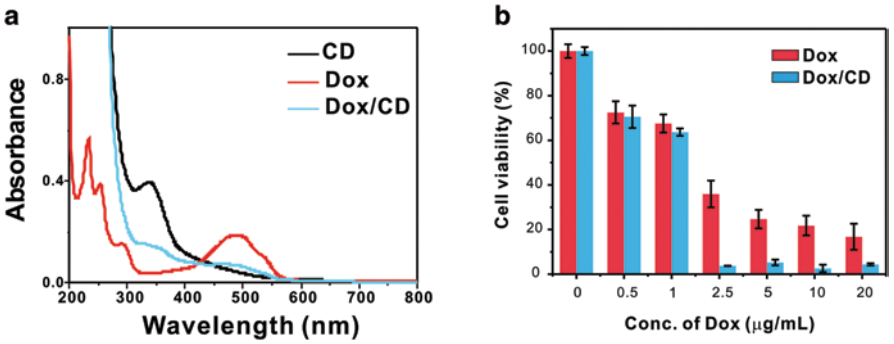

Fig. 10.16 **a** UV–vis absorbance spectra of CDs, Dox, and Dox-loaded CDs (Dox/CD). **b** Cell viability of the HeLa cancer cells exposed to different concentrations of Dox alone and Dox/CD (μg/mL) for 24 h

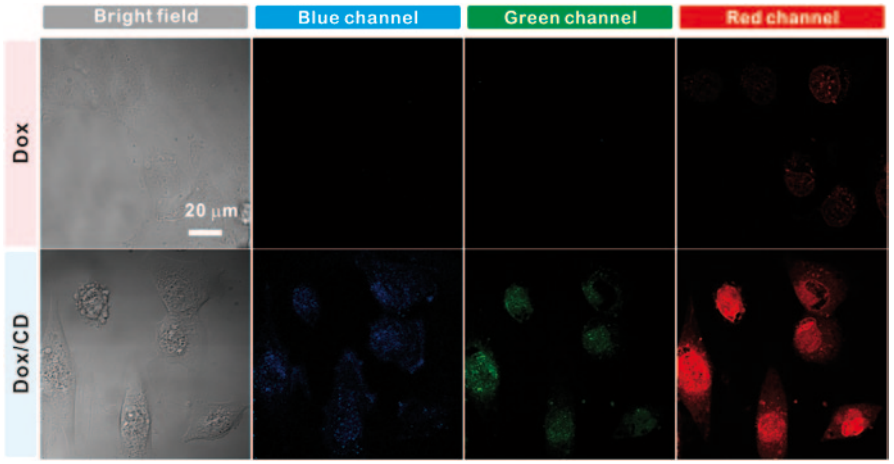

Fig. 10.17 Bright-field and confocal fluorescence images of HeLa cells treated with Dox and Dox/CD (2 μg/mL) for 24 h. Dox/CD delivers Dox to the nucleus more efficiently than Dox alone

considerably improved the therapeutic efficacy through CD-aided delivery, as compared to free Dox (Fig. 10.16b).

Enhanced Dox uptake by the CD carrier was confirmed by monitoring prominent red Dox fluorescence in the nucleus ($\lambda_{ex/em}$ = 480/520–640 nm) under a fluorescence microscope (Fig. 10.17). However, the cells treated with Dox alone showed weak fluorescence in the red channel. Therefore, the Dox/CD complex delivered Dox to the nucleus more efficiently than Dox alone, thereby suppressing cancer cell proliferation and acting as a fluorescent label for intracellular monitoring.

The nanoparticles with zwitterionic surfaces have shown higher colloidal stability over a wide pH range and reduced nonspecific interactions with serum components, thereby prolonging blood circulation for enhanced tumor accumulation